

Ferroelectric topological superconductor: α -In₂Se₃Xiaoming Zhang,^{1,*} Pei Zhao,¹ and Feng Liu^{2,†}¹*College of Physics and Optoelectronic Engineering, Ocean University of China, Qingdao, Shandong 266100, China*²*Department of Materials Science and Engineering, University of Utah, Salt Lake City, Utah 84112, USA* (Received 4 September 2023; revised 16 February 2024; accepted 26 February 2024; published 18 March 2024)

A two-dimensional topological superconductor (TSC) represents an exotic quantum material with quasiparticle excitation manifesting in dispersive Majorana modes (DMMs) at the boundaries. A domain-wall DMM can arise at the boundary between two TSC domains with opposite Chern numbers or with a π -phase shift in their pairing gap, which can only be tuned by a magnetic field. Here we propose the concept of a ferroelectric (FE) TSC, which not only enriches the domain-wall DMMs but also significantly makes them electrically tunable. The π -phase shift of the pairing gap is shown to be attained between two TSC domains of opposite FE polarization, and switchable by reversing FE polarizations. In combination with ferromagnetic (FM) polarization, the domain wall can host helical, doubled chiral, and fused DMMs, which can be transferred into each other by changing the direction of the electrical and/or magnetic field. Furthermore, based on first-principles calculations, we demonstrate α -In₂Se₃ to be a promising FE TSC candidate in proximity with a FM layer and a superconductor substrate. We envision that a FE TSC will significantly ease the manipulation of a DMM by electrical field to realize fault-tolerant quantum computation.

DOI: [10.1103/PhysRevB.109.125130](https://doi.org/10.1103/PhysRevB.109.125130)**I. INTRODUCTION**

A topological superconductor (TSC) represents an attractive condensed-matter system that can manifest an analogous form of a long-sought Majorana fermion [1,2]. A two-dimensional (2D) TSC is featured with one-dimensional (1D) dispersive Majorana modes (DMMs) at the boundaries, whose transport-induced non-Abelian braiding statistics offers a promising route to fault-tolerant quantum computing [3–5]. An intrinsic TSC phase at the weak pairing limit of spin-triplet p -wave superconductivity (SC) is characterized by an odd-parity pairing (OPP) gap [6,7], but occurs rarely in nature. Alternatively, an effective OPP gap can arise extrinsically from the constructive interplay between magnetic field, s -wave pairing gap, and spin-momentum-locked states, which have attracted much recent attention [8–15]. In addition to an outer boundary, the DMMs may arise at an inner boundary between two TSC domains with opposite Chern numbers or with a π -phase shift in their OPP gap, and can only be tuned by switching the ferromagnetic (FM) field. Here, we propose the concept of 2D ferroelectric (FE) TSCs, rendering a TSC platform that enables the domain-wall DMMs to be electrically tunable.

DMMs exhibiting distinct transport characteristics can be engineered by magnetic field in various existing TSC platforms. The extrinsic TSC phase was initiated by placing superconductors on surface of three-dimensional (3D) topological insulators (TIs) [8], which induces helical DMMs around the interface where an s -wave pairing gap receives a

π -phase shift [Fig. 1(a)], i.e., the gaps having opposite sign. The π -phase shift has been achieved by some clever and delicate experimental designs, such as by controlling magnetic flux through a SC loop in a Josephson junction [16,17], engineering the width and magnetization in the SC–FM–SC junction [18,19], or by shifting exactly half a unit cell of FeSe_{0.45}Te_{0.55} lattice [20,21]. The helical DMMs will evolve into chiral ones when time-reversal symmetry is broken by interfacing with a FM film, which leads to rich TSC phases tuned by magnetic field [9,10,22,23], and a fused domain-wall DMM could arise at the interface of two TSC domains of opposite Chern number or FM field [Fig. 1(b)]. Evidence of chiral DMMs has been observed in the magnetic TI (Cr_{0.12}Bi_{0.26}Sb_{0.62})₂Te₃ grown on Nb substrate [24]. Another TSC scheme replaces the 3D TI with a 2D noncentrosymmetric material exploiting the Rashba spin-orbit coupling (SOC) effect [11–13], which is again only magnetically tunable as the Rashba SOC in a given noncentrosymmetric material is fixed. Since the Rashba SOC naturally arises at the interface, a simplified TSC platform for this scheme is to place a FM Shiba lattice on a SC substrate [14,15], whose chiral DMMs are experimentally confirmed in heterostructures, including Pb/Co/Si(111) [25], Fe/Re(0001)-O(2 × 1) [26], and CrBr₃/NbSe₂ [27], via proximity effect.

In this paper, we demonstrate a unique class D TSC platform realized by a FE layer with the proximity effects of FM layer and SC substrate [Figs. 1(c) and 1(d)], so that the switchable FE polarization endows the FE TSC with a tunable Rashba SOC. Interestingly, we found that the chirality of SOC plays the same role as the π -phase shift of s -wave pairing in changing the sign of an OPP gap, because the spin-momentum-locked states have also a sense of sign to distinguish their chiral spin textures. However, the spin texture

*Corresponding author: zxm@ouc.edu.cn†Corresponding author: fliu@eng.utah.edu

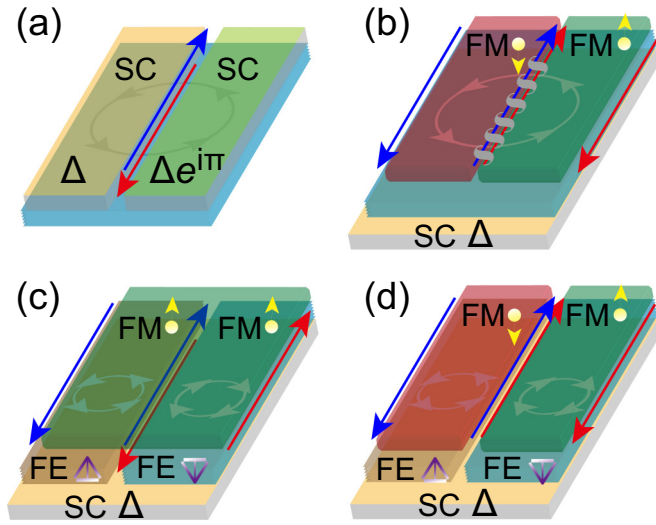


FIG. 1. Representative TSC platforms with tunable DMMs. (a) The helical DMMs realized by adding a π -phase shift to the pairing gap Δ of SC. (b) The fused and chiral DMMs realized by opposite FM fields under a uniform pairing gap. (c) The helical and chiral DMMs realized by opposite FE polarizations under a uniform pairing gap and FM field. (d) The doubled and chiral DMMs realized by opposite FE polarizations and opposite FE fields under a uniform pairing gap. The DMMs are plotted by red and blue lines with the arrow indicating the transport direction. The dot with a yellow arrow shows the direction of the FM field and the bar with a purple arrow shows the direction of the FE polarization. The gray circle with arrows represents the spin-momentum-locked states with specific chirality. The wrapped DMMs at the FM-FM domain wall in (b) denotes the fused DMMs.

is generally fixed for a given material or an existing TSC platform. In contrast, FE TSC enables the sign of OPP to be easily switched by reversing the chirality of the Rashba SOC via FE polarization, namely, by electrical field. Together with the sign of Chern number C controlled by FM polarization, there can be four different TSC domains having different sign combinations of OPP and C . Remarkably, depending on the FE/FM field configurations of adjacent domains, the domain wall can host helical [Fig. 1(c)], doubled chiral [Fig. 1(d)], and fused DMMs [Fig. 1(b)], which can be transferred into each other by reversing the electrical and/or magnetic field. Such high tunability may facilitate different braiding operations by engineering the location of domain walls and the DMM transport properties and even moving the domain-wall DMM by applying a dynamic field. Lastly, we confirm our theoretical model by first-principles calculations demonstrating an α - In_2Se_3 -based FE TSC in proximity with a FM layer and a SC substrate.

II. RESULTS

A. Theoretical model of FE TSC

We will recast the effective OPP theory originally based on Rashba SOC [11–15] in the framework of FE TSC by constructing a single-orbital tight-binding (TB) model on a

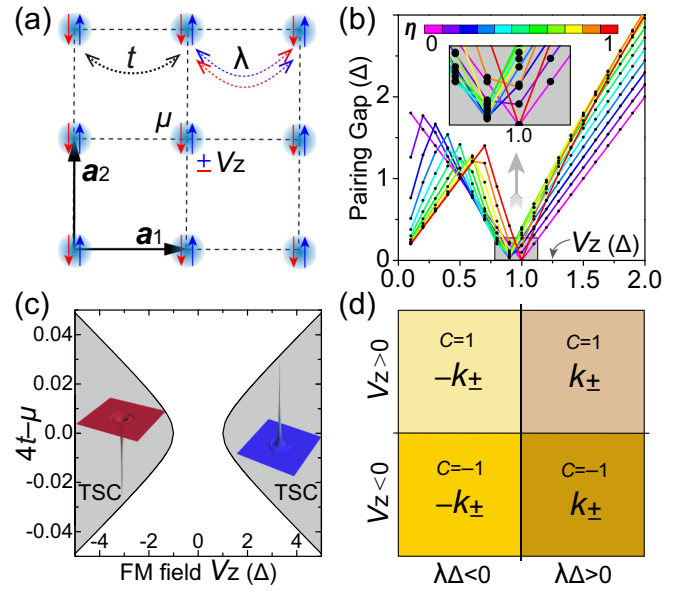


FIG. 2. FE TSC TB model analysis. (a) Schematics of the TB model on a square lattice. (b) FM field V_z -dependent pairing gap at $\mathbf{k} = 0$ calculated by diagonalizing $H_{\text{BdG}}^{h\alpha}(\mathbf{k})$ with different η . Inset is the magnified view near the FE TSC phase transition. The used parameters are $\mu = 4t$, $\Delta = 0.1t$, and $\lambda = 0.5t$. V_z is in the unit of Δ . (c) FE TSC phase diagram in the parameter space of V_z and $4t - \mu$. The left and right insets show the distribution of Berry curvature with $V_z < 0$ and $V_z > 0$, respectively. (d) Four FE TSC domains with different sign combinations of OPP and C .

square lattice [Fig. 2(a)]. Under the basis of $\phi_{\mathbf{k}} = (c_{\mathbf{k}\uparrow}, c_{\mathbf{k}\downarrow})^T$, the TB Hamiltonian is

$$h = \sum_{\mathbf{k}} \phi_{\mathbf{k}}^{\dagger} h(\mathbf{k}) \phi_{\mathbf{k}} \quad \text{with} \quad h(\mathbf{k}) = \epsilon_{\mathbf{k}} + V_z \sigma_z + 2\lambda \mathbf{g}_{\mathbf{k}} \cdot \boldsymbol{\sigma}, \quad (1)$$

where $c_{\mathbf{k}\alpha}$ ($c_{\mathbf{k}\alpha}^{\dagger}$) annihilates (creates) an electron with spin α and momentum \mathbf{k} . $\mathbf{k} = (k_x, k_y)$, $\epsilon_{\mathbf{k}} = 2t(\cos k_x + \cos k_y) - \mu$, $\mathbf{g}_{\mathbf{k}} = (\sin k_y, -\sin k_x)$, $\boldsymbol{\sigma} = (\sigma_x, \sigma_y)$. σ_i ($i = x, y, z$) denotes the Pauli matrices. t and μ are, respectively, the nearest-neighbor electron hopping and chemical potential. λ represents the strength of the built-in FE field and V_z is the external FM field. The reversal of the FE (FM) field is modeled by changing the sign of λ (V_z). $\mathbf{g}_{\mathbf{k}} \cdot \boldsymbol{\sigma}$ describes the spin-momentum locking induced by Rashba SOC. We note that Eq. (1) looks explicitly in the same form as previously developed for the Rashba SOC effect in noncentrosymmetric materials [11–15], but implicitly different because the sign of λ is tunable here but fixed before. This difference can lead to physical phenomena with significant practical implications, in particular the domain-wall DMM between two opposite FE domains that can be further tuned by an external electric field, as we elaborate below.

Then the Bogoliubov–de Gennes (BdG) Hamiltonian is constructed to describe the superconducting states under the Nambu basis of $\psi_{\mathbf{k}} = (c_{\mathbf{k}\uparrow}, c_{\mathbf{k}\downarrow}, c_{-\mathbf{k}\uparrow}^{\dagger}, c_{-\mathbf{k}\downarrow}^{\dagger})^T$:

$$H_{\text{BdG}} = \frac{1}{2} \sum_{\mathbf{k}} \psi_{\mathbf{k}}^{\dagger} H_{\text{BdG}}(\mathbf{k}) \psi_{\mathbf{k}}$$

with

$$H_{\text{BdG}}(\mathbf{k}) = \begin{pmatrix} \epsilon_{\mathbf{k}} + V_z & 2i\lambda k_- & 0 & \Delta \\ -2i\lambda k_+ & \epsilon_{\mathbf{k}} - V_z & -\Delta & 0 \\ 0 & -\Delta & -\epsilon_{\mathbf{k}} - V_z & -2i\lambda k_+ \\ \Delta & 0 & 2i\lambda k_- & -\epsilon_{\mathbf{k}} + V_z \end{pmatrix}, \quad (2)$$

where $k_{\pm} = \sin k_x \pm i \sin k_y$. The s -wave pairing potential Δ takes positive real values. The $H_{\text{BdG}}(\mathbf{k})$ can be transformed into the partitioned matrices $H_{\text{BdG}}^{t\alpha}(\mathbf{k}) = T_{l\alpha} H_{\text{BdG}}(\mathbf{k}) T_{r\alpha}$ with

$$H_{\text{BdG}}^{t\alpha}(\mathbf{k}) = \frac{1}{\epsilon_{\mathbf{k}} - V_z} \begin{pmatrix} \xi_{\mathbf{k}} & 4i\lambda\Delta k_- & 0 & 0 \\ -4i\lambda\Delta k_+ & -\xi_{\mathbf{k}} & 0 & 0 \\ 0 & 0 & (\epsilon_{\mathbf{k}} - V_z)^2 & 0 \\ 0 & 0 & 0 & -(\epsilon_{\mathbf{k}} - V_z)^2 \end{pmatrix}, \quad (3)$$

$$T_{l\alpha} = \frac{1}{\epsilon_{\mathbf{k}} - V_z} \begin{pmatrix} \epsilon_{\mathbf{k}} - V_z & -2i\lambda k_- & 0 & \Delta \\ 0 & \Delta & \epsilon_{\mathbf{k}} - V_z & -2i\lambda k_+ \\ 0 & \epsilon_{\mathbf{k}} - V_z & 0 & 0 \\ 0 & 0 & 0 & \epsilon_{\mathbf{k}} - V_z \end{pmatrix}, \quad (4)$$

$$T_{r\alpha} = \frac{1}{\epsilon_{\mathbf{k}} - V_z} \begin{pmatrix} \epsilon_{\mathbf{k}} - V_z & 0 & 0 & 0 \\ 2i\lambda k_+ & \Delta & \epsilon_{\mathbf{k}} - V_z & 0 \\ 0 & \epsilon_{\mathbf{k}} - V_z & 0 & 0 \\ \Delta & 2i\lambda k_- & 0 & \epsilon_{\mathbf{k}} - V_z \end{pmatrix}. \quad (5)$$

Here $\xi_{\mathbf{k}} = \epsilon_{\mathbf{k}}^2 + \Delta^2 - V_z^2 - 4\lambda^2 k_+ k_-$ and the basis of $H_{\text{BdG}}^{t\alpha}(\mathbf{k})$ is $\psi_{\mathbf{k}}^{t\alpha} = (c_{\mathbf{k}\uparrow}, c_{-\mathbf{k}\uparrow}^\dagger, c_{\mathbf{k}\downarrow} - \frac{2i\lambda k_+ c_{\mathbf{k}\uparrow} + \Delta c_{-\mathbf{k}\uparrow}^\dagger}{\epsilon_{\mathbf{k}} - V_z}, c_{-\mathbf{k}\downarrow}^\dagger - \frac{2i\lambda k_- c_{\mathbf{k}\uparrow}^\dagger + \Delta c_{\mathbf{k}\uparrow}}{\epsilon_{\mathbf{k}} - V_z})^T$. It should be pointed out that the requirement of $\epsilon_{\mathbf{k}} - V_z \neq 0$ for Eqs. (3)–(5) makes the above transformation only be well defined for $V_z > 0$ when $4t = \mu$. For $V_z < 0$, the transformation is redefined as $H_{\text{BdG}}^{t\beta}(\mathbf{k}) = T_{l\beta} H_{\text{BdG}}(\mathbf{k}) T_{r\beta}$ with

$$H_{\text{BdG}}^{t\beta}(\mathbf{k}) = \frac{1}{\epsilon_{\mathbf{k}} + V_z} \begin{pmatrix} (\epsilon_{\mathbf{k}} + V_z)^2 & 0 & 0 & 0 \\ 0 & -(\epsilon_{\mathbf{k}} + V_z)^2 & 0 & 0 \\ 0 & 0 & \xi_{\mathbf{k}} & 4i\lambda\Delta k_+ \\ 0 & 0 & -4i\lambda\Delta k_- & -\xi_{\mathbf{k}} \end{pmatrix}, \quad (6)$$

$$T_{l\beta} = \frac{1}{\epsilon_{\mathbf{k}} + V_z} \begin{pmatrix} \epsilon_{\mathbf{k}} + V_z & 0 & 0 & 0 \\ 0 & 0 & \epsilon_{\mathbf{k}} + V_z & 0 \\ 2i\lambda k_+ & \epsilon_{\mathbf{k}} + V_z & -\Delta & 0 \\ -\Delta & 0 & 2i\lambda k_- & \epsilon_{\mathbf{k}} + V_z \end{pmatrix}, \quad (7)$$

$$T_{r\beta} = \frac{1}{\epsilon_{\mathbf{k}} + V_z} \begin{pmatrix} \epsilon_{\mathbf{k}} + V_z & 0 & -2i\lambda k_- & -\Delta \\ 0 & 0 & \epsilon_{\mathbf{k}} + V_z & 0 \\ 0 & \epsilon_{\mathbf{k}} + V_z & -\Delta & -2i\lambda k_+ \\ 0 & 0 & 0 & \epsilon_{\mathbf{k}} + V_z \end{pmatrix}. \quad (8)$$

Here the basis of $H_{\text{BdG}}^{t\beta}(\mathbf{k})$ is $\psi_{\mathbf{k}}^{t\beta} = (c_{\mathbf{k}\uparrow} + \frac{2i\lambda k_- c_{\mathbf{k}\downarrow} + \Delta c_{-\mathbf{k}\downarrow}^\dagger}{\epsilon_{\mathbf{k}} + V_z}, c_{-\mathbf{k}\uparrow}^\dagger + \frac{2i\lambda k_+ c_{-\mathbf{k}\downarrow}^\dagger + \Delta c_{\mathbf{k}\downarrow}}{\epsilon_{\mathbf{k}} + V_z}, c_{\mathbf{k}\downarrow}, c_{-\mathbf{k}\downarrow}^\dagger)^T$.

One can easily realize that the submatrix $\begin{pmatrix} \xi_{\mathbf{k}} & 4i\lambda\Delta k_+ \\ -4i\lambda\Delta k_- & -\xi_{\mathbf{k}} \end{pmatrix}$ of $H_{\text{BdG}}^{t\alpha}(\mathbf{k})$ or $\begin{pmatrix} \xi_{\mathbf{k}} & 4i\lambda\Delta k_+ \\ -4i\lambda\Delta k_- & -\xi_{\mathbf{k}} \end{pmatrix}$ of $H_{\text{BdG}}^{t\beta}(\mathbf{k})$ describes a p -wave TSC having the OPP Ξk_{\pm} within the up- or down-spin component, respectively; here $\Xi = \text{sgn}(\lambda\Delta)$ and the subscript “ \pm ” indicating a time-reversal pair of degenerate chiral states. A TSC phase emerges at the weak pairing limit for the effective OPP [6,7], i.e., $\xi_{\mathbf{k}} < 0$ at the center of the Brillouin zone ($\mathbf{k} = 0$); it corresponds to the TSC phase transition condition of $(4t - \mu)^2 + \Delta^2 < V_z^2$.

Notice that the above transformations of the BdG Hamiltonian are not a unitary transformation because $T_{l\alpha} \neq T_{r\alpha}^{-1}$ (or $T_{l\beta} \neq T_{r\beta}^{-1}$); the eigenvalues of $H_{\text{BdG}}^{t\alpha}(\mathbf{k})$ [or $H_{\text{BdG}}^{t\beta}(\mathbf{k})$] and $H_{\text{BdG}}(\mathbf{k})$ are different. When $H_{\text{BdG}}(\mathbf{k})$ is gradually transformed into $H_{\text{BdG}}^{t\alpha}(\mathbf{k})$ [or $H_{\text{BdG}}^{t\beta}(\mathbf{k})$], the varying eigenvalues can be numerically traced by constructing a hypothetical Hamiltonian, $H_{\text{BdG}}^{h\alpha}(\mathbf{k}) = (1 - \eta)H_{\text{BdG}}(\mathbf{k}) + \eta H_{\text{BdG}}^{t\alpha}(\mathbf{k})$ [or $H_{\text{BdG}}^{h\beta}(\mathbf{k}) = (1 - \eta)H_{\text{BdG}}(\mathbf{k}) + \eta H_{\text{BdG}}^{t\beta}(\mathbf{k})$]. By diagonalizing the $H_{\text{BdG}}^{h\alpha}(\mathbf{k})$, as an example, we calculate the pairing gap at $\mathbf{k} = 0$ as a function of FM field V_z for different η and setting $4t - \mu = 0$ [Fig. 2(b)]. One can clearly see a gap reopening process with the increasing V_z , where the gap closes at $V_z = \Delta$ for both $\eta = 0.0$ and $\eta = 1.0$, but the gap never

closes when η is varied from 0.0 to 1.0 for a given V_z . This can also be captured from the different band dispersions of superconducting quasiparticles when η varies from 0.0 to 1.0 for the trivial SC phase [Fig. S1(a)], at the critical point of phase transition [Fig. S1(b)], and for the FE TSC phase [Fig. S1(c)], respectively, in the Supplemental Material (SM) [28], which includes Refs. [29–34]. This indicates that the pairing gaps of $H_{\text{BdG}}(\mathbf{k})$ and $H_{\text{BdG}}^{h\alpha}(\mathbf{k})$ are adiabatically connected belonging to the same topological class. The same conclusion can be drawn for $H_{\text{BdG}}^{h\beta}(\mathbf{k})$. Thus, the FE TSC phase described by $H_{\text{BdG}}(\mathbf{k})$ will emerge under the condition $(4t - \mu)^2 + \Delta^2 < V_z^2$ [Fig. 2(c)]. Given that $4t$ is the energy of the Kramers pair at $\mathbf{k} = 0$, the condition derived here for the TSC phase transition is consistent with previous reports [11–13].

B. DMMs of FE TSC tuned by electrical and magnetic field

A critical insight from the FE TSC TB model is that the effective OPP gap possesses the form of Ξk_{\pm} with $\Xi = \text{sgn}(\lambda\Delta)$, meaning the sign of the OPP gap depends on the sign of λ , in addition to the phase of the s -wave pairing gap. Thus, the OPP symmetry of k_{\pm} and $-k_{\pm}$ can be interchanged by either attaching a π phase to the pairing gap, which is well known before, or reversing the sign of λ , as we propose here. Together with different signs of C [Fig. 2(c)], there are four FE TSC domains that can be achieved and distinguished by different C and/or OPP [Fig. 2(d)]. Here the Chern number C depends on the direction of the FM field, because the positive and negative V_z endows the effective OPP gap condensing on different spin components [see Eqs. (3) and (6)]. This fact can be further confirmed by integrating the Berry curvature of the BdG quasiparticle wave function below the pairing gap [see insets of Fig. 2(c)], which leads to $C = \text{sgn}(V_z)$.

In conventional TSC platforms, the sign of λ is not changeable; while here for the FE TSC, we generalize the TSC domains by including also the sign of λ or the OPP gap. The four FE TSC domains [Fig. 2(d)] will lead to 4^N configurations for a system with N FE and/or FM domains, where the domain-wall boundaries interfacing different TSC domains host a rich variety of DMMs. The domain walls can be formed between FE domains of opposite polarization, FM domains of opposite magnetization, and their combinations, which we abbreviate as the FE-FE, FM-FM, and FE/FM-FE/FM domain wall, respectively. As an example, we consider a FE TSC nanoribbon made of two domains denoted by (V_z^l, λ^l) and (V_z^r, λ^r) on the left and right, respectively, as shown in Fig. 3(a). By changing the signs of these four parameters, 16 configurations can be divided into four categories based on the chirality and location of DMMs, each consisting of four configurations.

The first category has the left and right domains of the same TSC phase, which requires $\text{sgn}(V_z^l) = \text{sgn}(V_z^r)$ and $\text{sgn}(\lambda^l) = \text{sgn}(\lambda^r)$. There is only the outer-edge DMMs whose transport direction can be reversed by changing the FM field direction (see Fig. S2 in the SM [28]). The second category has the interface between two FE TSC domains with opposite sign of both C and λ . The domain walls in this category host two chiral DMMs, transporting in opposite directions of the two chiral DMMs at the right and left outer edges [see Fig. 3(b),

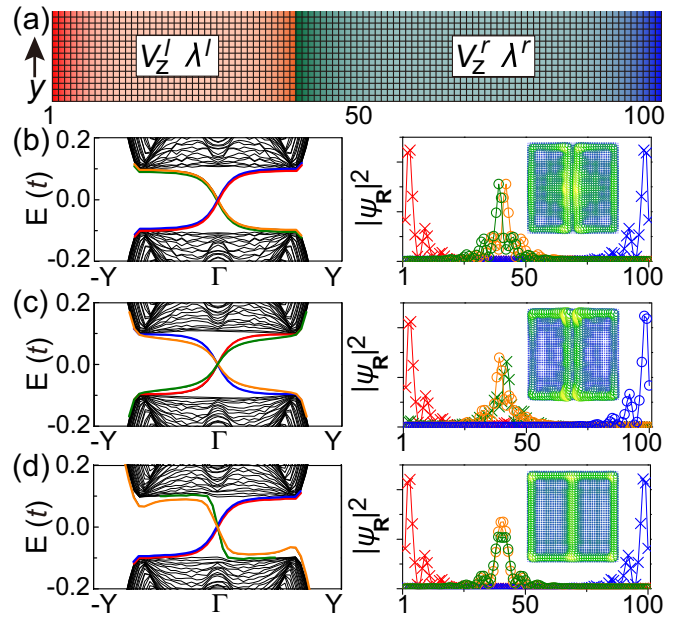


FIG. 3. DMMs with high tunability. (a) Schematics of a nanoribbon, with (V_z^l, λ^l) and (V_z^r, λ^r) marking the left and right domains, respectively. The width of the left (right) domain is 40 (60) unit cells and the arrow y indicates the periodic direction. (b)–(d) Nanoribbon BdG quasiparticle band structure (left panel) and real-space DMM distribution $|\psi_{\mathbf{R}}|^2$ (right panel) calculated for the left (right) domain configurations of (b) $\{V_z^l, \lambda^l\}$ ($\{V_z^r, \lambda^r\}$) or $\{V_z^l, \lambda^l\}$ ($\{V_z^r, \lambda^r\}$), (c) $\{V_z^l, \lambda^l\}$ ($\{V_z^r, \lambda^r\}$) or $\{V_z^l, \lambda^l\}$ ($\{V_z^r, \lambda^r\}$), and (d) $\{V_z^l, \lambda^l\}$ ($\{V_z^r, \lambda^r\}$) or $\{V_z^l, \lambda^l\}$ ($\{V_z^r, \lambda^r\}$), respectively. We use curly braces to show the combinations of V_z and λ , whose sign is indicated by the subscript $+$ or $-$. The DMMs inside the pairing gap (left panels) and the corresponding real-space distributions (right panels) are plotted in the same color. Crosses and circles indicate the DMMs transporting in the $+y$ and $-y$ direction, respectively. Insets are the distributions of the DMMs in a square island of FE TSC with a domain wall in the middle.

and Fig. S3(a) in the SM [28]). The location of DMMs is determined by calculating their probability density $|\psi_{\mathbf{R}}|^2$ in real space and the transport direction is identified by their Fermi velocity. The third category has the interface between two FE TSC domains with the same C and opposite sign of λ , which is characterized with chiral DMMs transporting oppositely at two outer edges and helical DMMs at the inner FE-FE domain wall [see Fig. 3(c), and Fig. S3(b) in the SM [28]]. The helical DMMs are similar to the ones around the interface where an s -wave pairing gap receives a π -phase shift on the surface of TI [6], but formed by interfacing two TSC domains of the same Chern number but with opposite FE polarization that induces a π -phase difference in their pairing gap. The last category is interfaced by two FE TSC domains with opposite sign of C and same sign of OPP λ . The transport of their domain-wall DMMs looks like that of the second category except the wave functions of two DMMs at the FM-FM domain wall hybridize [see Fig. 3(d), and Fig. S3(c) in the SM [28]], forming fused DMMs. Clearly, in addition to FM, FE polarization provides another maneuverable knob to tune the transport of DMMs for FE TSCs, which is robust against

fluctuations around the domain wall (see Note S1 of the SM [28]).

C. First-principles calculation of α -In₂Se₃-based FE TSC

FEs are well-known functional materials with spontaneous FE polarization switchable by an external electrical field. Recently, 2D FE materials have received increasing attention and been extensively explored in layered van der Waals materials [35–37], including the experimentally verified CuInP₂S₆ [38], SnTe [39], SnS [40], α -In₂Se₃ [41–43], β -In₂Se₃ [44], β' -In₂Se₃ [45], $d1T$ -MoTe₂ [46], $1T'$ -MoS₂ layers [47], sliding $1T'$ -ReS₂ multilayers [48], $1T'$ -WTe₂ trilayer [49], T_d -WTe₂ bilayer [50], $1H$ TMD multilayers [51], few-layer InSe [52], stacked bilayer boron nitride (BN) [53,54], BN/Bernal-stacked bilayer graphene/BN [55], etc. Here we focus on demonstrating an α -In₂Se₃-based FE TSC, as an example to implement our theoretical prediction.

The α -In₂Se₃ monolayer consists of five atomic planes (Se-In-Se-In-Se), where the shifting of the central Se plane reverses the out-of-plane FE polarization [Fig. S8(a) in the SM [28]]. First-principles calculations (see Note S2 of the SM [28]) show the polarization leads to spin splitting of bands [Fig. S8(b) in the SM [28]] and opposite FE polarization can be distinguished from the distribution of spin expectation values in momentum space. Taking the lowest conduction band as an example, one can see the chirality of spin textures is opposite for the upward [Fig. S8(c) in the SM [28]] and downward [Fig. S8(d) in the SM [28]] FE polarization. This switchable chirality is what simulated in our TB model by changing the sign of λ .

Since electrons can be doped by gating [56] or a built-in depolarization field [57] in α -In₂Se₃, we consider the s -wave pairing condensed in the conduction band of α -In₂Se₃ near the Γ point upon the proximity effect with a superconductor substrate. We concretely demonstrate different TSC domains by considering a nanoribbon made of α -In₂Se₃ with opposite FE polarizations at right and left domains [Fig. 4(a)], while a magnetic field can be induced by interfacing with a FM layer [58–62]. By constructing a first-principles BdG Hamiltonian based on Wannier functions (see Note S3 of the SM [28]), we successfully reproduce the DMMs at the FE/FM-FE/FM [Fig. 4(b)] and FE-FE [Fig. 4(c)] domain walls, whose transport features and distributions are in excellent agreement with the TB model calculations [Figs. 3(b) and 3(c)].

III. DISCUSSION AND PERSPECTIVE

In general, a FE TSC requires a FE metallic state with preferably large SOC. Recent progress has been made in 2D FE metals [63–65], and gating may be applied to dope the FE semiconductor into a metallic state, such as α -In₂Se₃ [56,57], bilayer T_d -WTe₂ [50], and multilayer WSe₂ or MoS₂ [51]. Another requirement is introducing SC into the FE layer via proximity effect, which has been long shown experimentally [66,67]. In addition, experiments have made FE/SC heterostructures with FE layer modulating SC in bilayer T_d -MoTe₂ [68], Pb(Zr_xTi_{1-x})O₃/GdBa₂Cu₃O_{7-x} [69], Nb-doped SrTiO₃/Pb(Zr,Ti)O₃ [70], and BiFeO₃/YBa₂Cu₃O_{7- δ} [71], which indirectly support our proposal. The last

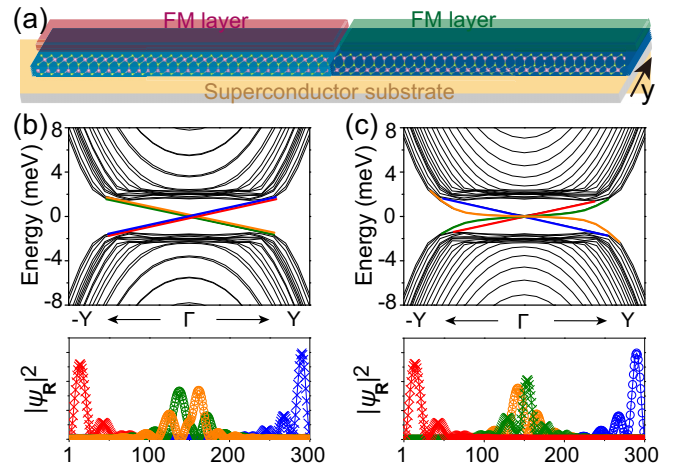


FIG. 4. Characterization of α -In₂Se₃-based FE TSC. (a) Schematic diagram of α -In₂Se₃-based FE TSC nanoribbon with opposite FE polarizations at the left and right domains. (b),(c) Nanoribbon BdG quasiparticle band structure (upper panel) and real-space DMM distribution $|\psi_R|^2$ (lower panel) calculated for the nanoribbon with (b) opposite and (c) uniform FM fields at left and right domains. The DMMs inside the pairing gap (upper panels) and the corresponding real-space distributions (lower panels) are plotted using the same color. $|\psi_R|^2$ peaks around the outer edges (position 1 or 300) and around the inner domain wall (position 150). Symbols of crosses and circles indicate the DMMs transporting in the $+y$ and $-y$ direction, respectively.

requirement is the FM field V_z , with tunable magnitude and direction, which is expected to be acquired by coupling FEs with FMs via heterostructures formed by vastly available FE and FM candidates [58–62]. Moreover, we expect that stoichiometric 2D multiferroics is also plausible to trigger the FE TSC phase. Given the experimental realization of multiferroicity in CuCrP₂S₆ [72], distorted monolayer ReS₂ [73], iron-doped α -In₂Se₃ [74], single atomic layer of NiI₂ [75], atomically thin ϵ -Fe₂O₃ [76], and oxide-based 2D electron gas [77], we suggest future efforts to be made along this direction.

Because intrinsic TSCs are very rare, much recent attention has been paid to extrinsic TSCs employing the proximity effect [8–15]. While the existence of TSCs and DMMs has been experimentally confirmed [24–27], our proposed FE TSC paves the way to tuning the location, chirality, coupling, and motion of DMMs by using an electrical field, which should stimulate future efforts along this interesting and exciting direction. We point out that the FE TSC phases are not limited to the OPP gap of $\pm k_{\pm}$ we discuss here, because the polar point groups of FEs induce not only Rashba SOC, but also other forms of antisymmetric SOC and their mixtures [78]. This may further expand the diversity of OPP gaps, and hence the FE TSC domains. We also mention that the domain walls are actively explored in the field of “domain-wall nanoelectronics” [79] for potential applications of low-energy electronics in memory, logic, and brain-inspired neuromorphic computing. Here we propose domain-wall DMMs in FE TSCs, which may open a door to domain-wall quantum computation.

ACKNOWLEDGMENTS

X.Z. and P.Z. acknowledge the financial support by the National Natural Science Foundation of China (Grant No. 12004357), the Natural Science Foundation of Shandong

Province (Grant No. ZR2020QA053), and the Young Talents Project at Ocean University of China. F.L. acknowledges financial support from DOE-BES (Grant No. DE-FG02-04ER46148).

-
- [1] X.-L. Qi and S.-C. Zhang, Topological insulators and superconductors, *Rev. Mod. Phys.* **83**, 1057 (2011).
- [2] M. Sato and Y. Ando, Topological superconductors: A review, *Rep. Prog. Phys.* **80**, 076501 (2017).
- [3] Y. Hu and C. L. Kane, Fibonacci topological superconductor, *Phys. Rev. Lett.* **120**, 066801 (2018).
- [4] B. Lian, X.-Q. Sun, A. Vaezi, X.-L. Qi, and S.-C. Zhang, Topological quantum computation based on chiral Majorana fermions, *Proc. Natl. Acad. Sci. USA* **115**, 10938 (2018).
- [5] C. W. J. Beenakker, P. Baireuther, Y. Herasymenko, I. Adagideli, L. Wang, and A. R. Akhmerov, Deterministic creation and braiding of chiral edge vortices, *Phys. Rev. Lett.* **122**, 146803 (2019).
- [6] N. Read and D. Green, Paired states of fermions in two dimensions with breaking of parity and time-reversal symmetries and the fractional quantum Hall effect, *Phys. Rev. B* **61**, 10267 (2000).
- [7] A. Y. Kitaev, Unpaired Majorana fermions in quantum wires, *Phys.-Usp.* **44**, 131 (2001).
- [8] L. Fu and C. L. Kane, Superconducting proximity effect and Majorana fermions at the surface of a topological insulator, *Phys. Rev. Lett.* **100**, 096407 (2008).
- [9] X.-L. Qi, T. L. Hughes, and S.-C. Zhang, Chiral topological superconductor from the quantum Hall state, *Phys. Rev. B* **82**, 184516 (2010).
- [10] J. Wang, Q. Zhou, B. Lian, and S.-C. Zhang, Chiral topological superconductor and half-integer conductance plateau from quantum anomalous Hall plateau transition, *Phys. Rev. B* **92**, 064520 (2015).
- [11] M. Sato, Y. Takahashi, and S. Fujimoto, Non-Abelian topological order in s -wave superfluids of ultracold fermionic atoms, *Phys. Rev. Lett.* **103**, 020401 (2009).
- [12] J. D. Sau, R. M. Lutchyn, S. Tewari, and S. Das Sarma, Generic new platform for topological quantum computation using semiconductor heterostructures, *Phys. Rev. Lett.* **104**, 040502 (2010).
- [13] J. Alicea, Majorana fermions in a tunable semiconductor device, *Phys. Rev. B* **81**, 125318 (2010).
- [14] J. Röntynen and T. Ojanen, Topological superconductivity and high Chern numbers in 2D ferromagnetic Shiba lattices, *Phys. Rev. Lett.* **114**, 236803 (2015).
- [15] J. Li, T. Neupert, Z. Wang, A. H. MacDonald, A. Yazdani, and B. A. Bernevig, Two-dimensional chiral topological superconductivity in Shiba lattices, *Nat. Commun.* **7**, 12297 (2016).
- [16] A. Fornieri, A. M. Whiticar, F. Setiawan, E. Portolés, A. C. C. Drachmann, A. Keselman, S. Gronin, C. Thomas, T. Wang, R. Kallaher, G. C. Gardner, E. Berg, M. J. Manfra, A. Stern, C. M. Marcus, and F. Nichele, Evidence of topological superconductivity in planar Josephson junctions, *Nature (London)* **569**, 89 (2019).
- [17] H. Ren, F. Pientka, S. Hart, A. T. Pierce, M. Kosowsky, L. Lunczer, R. Schlereth, B. Scharf, E. M. Hankiewicz, L. W. Molenkamp, B. I. Halperin, and A. Yacoby, Topological superconductivity in a phase-controlled Josephson junction, *Nature (London)* **569**, 93 (2019).
- [18] S. Kawabata, Y. Asano, Y. Tanaka, A. A. Golubov, and S. Kashiwaya, Josephson π state in a ferromagnetic insulator, *Phys. Rev. Lett.* **104**, 117002 (2010).
- [19] C. Schrade, A. A. Zyuzin, J. Klinovaja, and D. Loss, Proximity-induced π Josephson junctions in topological insulators and Kramers pairs of Majorana fermions, *Phys. Rev. Lett.* **115**, 237001 (2015).
- [20] Z. Wang, J. O. Rodriguez, L. Jiao, S. Howard, M. Graham, G. D. Gu, T. L. Hughes, D. K. Morr, and V. Madhavan, Evidence for dispersing 1D Majorana channels in an iron-based superconductor, *Science* **367**, 104 (2020).
- [21] R. Song, P. Zhang, and N. Hao, Phase-manipulation-induced Majorana mode and braiding realization in iron-based superconductor Fe(Te,Se), *Phys. Rev. Lett.* **128**, 016402 (2022).
- [22] Y. Huang and C.-K. Chiu, Helical Majorana edge mode in a superconducting antiferromagnetic quantum spin Hall insulator, *Phys. Rev. B* **98**, 081412(R) (2018).
- [23] X. Zhang and F. Liu, Prediction of Majorana edge states from magnetized topological surface states, *Phys. Rev. B* **103**, 024405 (2021).
- [24] J. Shen, J. Lyu, J. Z. Gao, Y.-M. Xie, C.-Z. Chen, C.-w. Cho, O. Atanov, Z. Chen, K. Liu, Y. J. Hu, K. Y. Yip, S. K. Goh, Q. L. He, L. Pan, K. L. Wang, K. T. Law, and R. Lortz, Spectroscopic fingerprint of chiral Majorana modes at the edge of a quantum anomalous Hall insulator/superconductor heterostructure, *Proc. Natl. Acad. Sci. USA* **117**, 238 (2020).
- [25] G. C. Ménard, S. Guissart, C. Brun, R. T. Leriche, M. Trif, F. Debontridder, D. Demaille, D. Roditchev, P. Simon, and T. Cren, Two-dimensional topological superconductivity in Pb/Co/Si(111), *Nat. Commun.* **8**, 2040 (2017).
- [26] A. Palacio-Morales, E. Mascot, S. Cocklin, H. Kim, S. Rachel, D. K. Morr, and R. Wiesendanger, Atomic-scale interface engineering of Majorana edge modes in a 2D magnet-superconductor hybrid system, *Sci. Adv.* **5**, eaav6600 (2019).
- [27] S. Kezilebieke, M. N. Huda, V. Vaño, M. Aapro, S. C. Ganguli, O. J. Silveira, S. Głodzik, A. S. Foster, T. Ojanen, and P. Liljeroth, Topological superconductivity in a van der Waals heterostructure, *Nature (London)* **588**, 424 (2020).
- [28] See Supplemental Material at <http://link.aps.org/supplemental/10.1103/PhysRevB.109.125130> further discussions on the robustness of DMMs tuned by FM and/or FE polarization, details

- of first-principles calculations on α - In_2Se_3 -based FE TSC, and supplemental figures.
- [29] P. Hohenberg and W. Kohn, Inhomogeneous electron gas, *Phys. Rev.* **136**, B864 (1964).
- [30] W. Kohn and L. J. Sham, Self-consistent equations including exchange and correlation effects, *Phys. Rev.* **140**, A1133 (1965).
- [31] J. P. Perdew, K. Burke, and M. Ernzerhof, Generalized gradient approximation made simple, *Phys. Rev. Lett.* **77**, 3865 (1996).
- [32] P. E. Blöchl, Projector augmented-wave method, *Phys. Rev. B* **50**, 17953 (1994).
- [33] A. A. Mostofi, J. R. Yates, G. Pizzi, Y.-S. Lee, I. Souza, D. Vanderbilt, and N. Marzari, An updated version of wannier90: A tool for obtaining maximally-localised Wannier functions, *Comput. Phys. Commun.* **185**, 2309 (2014).
- [34] X. Zhang, K.-H. Jin, J. Mao, M. Zhao, Z. Liu, and F. Liu, Prediction of intrinsic topological superconductivity in Mn-doped GeTe monolayer from first-principles, *npj Comput. Mater.* **7**, 44 (2021).
- [35] D. Zhang, P. Schoenherr, P. Sharma, and J. Seidel, Ferroelectric order in van der Waals layered materials, *Nat. Rev. Mater.* **8**, 25 (2023).
- [36] M. Wu and J. Li, Sliding ferroelectricity in 2D van der Waals materials: Related physics and future opportunities, *Proc. Natl. Acad. Sci. USA* **118**, e2115703118 (2021).
- [37] L. Qi, S. Ruan, and Y.-J. Zeng, Review on recent developments in 2D ferroelectrics: Theories and applications, *Adv. Mater.* **33**, 2005098 (2021).
- [38] A. Belianinov, Q. He, A. Dziaugys, P. Maksymovych, E. Eliseev, A. Borisevich, A. Morozovska, J. Banys, Y. Vysochanskii, and S. V. Kalinin, CuInP_2S_6 room temperature layered ferroelectric, *Nano Lett.* **15**, 3808 (2015).
- [39] K. Chang, J. Liu, H. Lin, N. Wang, K. Zhao, A. Zhang, F. Jin, Y. Zhong, X. Hu, W. Duan, Q. Zhang, L. Fu, Q.-K. Xue, X. Chen, and S.-H. Ji, Discovery of robust in-plane ferroelectricity in atomic-thick SnTe , *Science* **353**, 274 (2016).
- [40] N. Higashitarumizu, H. Kawamoto, C.-J. Lee, B.-H. Lin, F.-H. Chu, I. Yonemori, T. Nishimura, K. Wakabayashi, W.-H. Chang, and K. Nagashio, Purely in-plane ferroelectricity in monolayer SnS at room temperature, *Nat. Commun.* **11**, 2428 (2020).
- [41] Y. Zhou, D. Wu, Y. Zhu, Y. Cho, Q. He, X. Yang, K. Herrera, Z. Chu, Y. Han, M. C. Downer, H. Peng, and K. Lai, Out-of-plane piezoelectricity and ferroelectricity in layered α - In_2Se_3 nanoflakes, *Nano Lett.* **17**, 5508 (2017).
- [42] C. Cui, W.-J. Hu, X. Yan, C. Addiego, W. Gao, Y. Wang, Z. Wang, L. Li, Y. Cheng, P. Li, X. Zhang, H. N. Alshareef, T. Wu, W. Zhu, X. Pan, and L.-J. Li, Intercorrelated in-plane and out-of-plane ferroelectricity in ultrathin two-dimensional layered semiconductor In_2Se_3 , *Nano Lett.* **18**, 1253 (2018).
- [43] J. Xiao, H. Zhu, Y. Wang, W. Feng, Y. Hu, A. Dasgupta, Y. Han, Y. Wang, D. A. Muller, L. W. Martin, P. Hu, and X. Zhang, Intrinsic two-dimensional ferroelectricity with dipole locking, *Phys. Rev. Lett.* **120**, 227601 (2018).
- [44] Z. Zhang, J. Nie, Z. Zhang, Y. Yuan, Y.-S. Fu, and W. Zhang, Atomic visualization and switching of ferroelectric order in β - In_2Se_3 films at the single layer limit, *Adv. Mater.* **34**, 2106951 (2022).
- [45] C. Zheng, L. Yu, L. Zhu, J. L. Collins, D. Kim, Y. Lou, C. Xu, M. Li, Z. Wei, Y. Zhang, M. T. Edmonds, S. Li, J. Seidel, Y. Zhu, J. Z. Liu, W.-X. Tang, and M. S. Fuhrer, Room temperature in-plane ferroelectricity in van der Waals In_2Se_3 , *Sci. Adv.* **4**, eaar7720 (2018).
- [46] S. Yuan, X. Luo, H. L. Chan, C. Xiao, Y. Dai, M. Xie, and J. Hao, Room-temperature ferroelectricity in MoTe_2 down to the atomic monolayer limit, *Nat. Commun.* **10**, 1775 (2019).
- [47] A. Lipatov, P. Chaudhary, Z. Guan, H. Lu, G. Li, O. Crégut, K. D. Dorkenoo, R. Proksch, S. Cherifi-Hertel, D.-F. Shao, E. Y. Tsybmal, J. Íñiguez, A. Sinitskii, and A. Gruverman, Direct observation of ferroelectricity in two-dimensional MoS_2 , *npj 2D Mater. Appl.* **6**, 18 (2022).
- [48] Y. Wan, T. Hu, X. Mao, J. Fu, K. Yuan, Y. Song, X. Gan, X. Xu, M. Xue, X. Cheng, C. Huang, J. Yang, L. Dai, H. Zeng, and E. Kan, Room-temperature ferroelectricity in $1T'$ - ReS_2 multilayers, *Phys. Rev. Lett.* **128**, 067601 (2022).
- [49] Z. Fei, W. Zhao, T. A. Palomaki, B. Sun, M. K. Miller, Z. Zhao, J. Yan, X. Xu, and D. H. Cobden, Ferroelectric switching of a two-dimensional metal, *Nature (London)* **560**, 336 (2018).
- [50] S. C. de la Barrera, Q. Cao, Y. Gao, Y. Gao, V. S. Bheemarasetty, J. Yan, D. G. Mandrus, W. Zhu, D. Xiao, and B. M. Hunt, Direct measurement of ferroelectric polarization in a tunable semimetal, *Nat. Commun.* **12**, 5298 (2021).
- [51] S. Deb, W. Cao, N. Raab, K. Watanabe, T. Taniguchi, M. Goldstein, L. Kronik, M. Urbakh, O. Hod, and M. Ben Shalom, Cumulative polarization in conductive interfacial ferroelectrics, *Nature (London)* **612**, 465 (2022).
- [52] H. Hu, H. Wang, Y. Sun, J. Li, J. Wei, D. Xie, and H. Zhu, Out-of-plane and in-plane ferroelectricity of atom-thick two-dimensional InSe , *Nanotechnology* **32**, 385202 (2021).
- [53] K. Yasuda, X. Wang, K. Watanabe, T. Taniguchi, and P. Jarillo-Herrero, Stacking-engineered ferroelectricity in bilayer boron nitride, *Science* **372**, 1458 (2021).
- [54] M. Vizner Stern, Y. Waschitz, W. Cao, I. Nevo, K. Watanabe, T. Taniguchi, E. Sela, M. Urbakh, O. Hod, and M. Ben Shalom, Interfacial ferroelectricity by van der Waals sliding, *Science* **372**, 1462 (2021).
- [55] Z. Zheng, Q. Ma, Z. Bi, S. de la Barrera, M.-H. Liu, N. Mao, Y. Zhang, N. Kiper, K. Watanabe, T. Taniguchi, J. Kong, W. A. Tisdale, R. Ashoori, N. Gedik, L. Fu, S.-Y. Xu, and P. Jarillo-Herrero, Unconventional ferroelectricity in moiré heterostructures, *Nature (London)* **588**, 71 (2020).
- [56] J. R. Rodriguez, W. Murray, K. Fujisawa, S. H. Lee, A. L. Kotrick, Y. Chen, N. McKee, S. Lee, M. Terrones, S. Trolier-McKinstry, T. N. Jackson, Z. Mao, Z. Liu, and Y. Liu, Electric field induced metallic behavior in thin crystals of ferroelectric α - In_2Se_3 , *Appl. Phys. Lett.* **117**, 052901 (2020).
- [57] C. Ke, J. Huang, and S. Liu, Two-dimensional ferroelectric metal for electrocatalysis, *Mater. Horizons* **8**, 3387 (2021).
- [58] W. Sun, W. Wang, D. Chen, Z. Cheng, and Y. Wang, Valence mediated tunable magnetism and electronic properties by ferroelectric polarization switching in 2D $\text{FeI}_2/\text{In}_2\text{Se}_3$ van der Waals heterostructures, *Nanoscale* **11**, 9931 (2019).
- [59] C. Gong, E. M. Kim, Y. Wang, G. Lee, and X. Zhang, Multiferroicity in atomic van der Waals heterostructures, *Nat. Commun.* **10**, 2657 (2019).
- [60] F. Xue, Z. Wang, Y. Hou, L. Gu, and R. Wu, Control of magnetic properties of MnBi_2Te_4 using a van der Waals ferroelectric $\text{III}_2\text{-VI}_3$ film and biaxial strain, *Phys. Rev. B* **101**, 184426 (2020).
- [61] B. Yang, B. Shao, J. Wang, Y. Li, C. Yam, S. Zhang, and B. Huang, Realization of semiconducting layered multiferroic

- heterojunctions via asymmetrical magnetoelectric coupling, *Phys. Rev. B* **103**, L201405 (2021).
- [62] K. Dou, W. Du, Y. Dai, B. Huang, and Y. Ma, Two-dimensional magnetoelectric multiferroics in a MnSTe/In₂Se₃ heterobilayer with ferroelectrically controllable skyrmions, *Phys. Rev. B* **105**, 205427 (2022).
- [63] W. X. Zhou and A. Ariando, Review on ferroelectric/polar metals, *Jpn. J. Appl. Phys.* **59**, S10802 (2020).
- [64] X.-Y. Ma, H.-Y. Lyu, K.-R. Hao, Y.-M. Zhao, X. Qian, Q.-B. Yan, and G. Su, Large family of two-dimensional ferroelectric metals discovered via machine learning, *Sci. Bull.* **66**, 233 (2021).
- [65] D. Hickox-Young, D. Puggioni, and J. M. Rondinelli, Polar metals taxonomy for materials classification and discovery, *Phys. Rev. Mater.* **7**, 010301 (2023).
- [66] C. Huang, B. T. Zhou, H. Zhang, B. Yang, R. Liu, H. Wang, Y. Wan, K. Huang, Z. Liao, E. Zhang, S. Liu, Q. Deng, Y. Chen, X. Han, J. Zou, X. Lin, Z. Han, Y. Wang, K. T. Law, and F. Xiu, Proximity-induced surface superconductivity in Dirac semimetal Cd₃As₂, *Nat. Commun.* **10**, 2217 (2019).
- [67] C. Li, Y.-F. Zhao, A. Vera, O. Lesser, H. Yi, S. Kumari, Z. Yan, C. Dong, T. Bowen, K. Wang, H. Wang, J. L. Thompson, K. Watanabe, T. Taniguchi, D. Reifsnnyder Hickey, Y. Oreg, J. A. Robinson, C.-Z. Chang, and J. Zhu, Proximity-induced superconductivity in epitaxial topological insulator/graphene/gallium heterostructures, *Nat. Mater.* **22**, 570 (2023).
- [68] A. Jindal, A. Saha, Z. Li, T. Taniguchi, K. Watanabe, J. C. Hone, T. Birol, R. M. Fernandes, C. R. Dean, A. N. Pasupathy, and D. A. Rhodes, Coupled ferroelectricity and superconductivity in bilayer $T_d - \text{MoTe}_2$, *Nature (London)* **613**, 48 (2023).
- [69] C. H. Ahn, S. Gariglio, P. Paruch, T. Tybell, L. Antognazza, and J. M. Triscone, Electrostatic modulation of superconductivity in ultrathin GdBa₂Cu₃O_{7-x} films, *Science* **284**, 1152 (1999).
- [70] K. S. Takahashi, M. Gabay, D. Jaccard, K. Shibuya, T. Ohnishi, M. Lippmaa, and J. M. Triscone, Local switching of two-dimensional superconductivity using the ferroelectric field effect, *Nature (London)* **441**, 195 (2006).
- [71] A. Crassous, R. Bernard, S. Fusil, K. Bouzehouane, D. Le Bourdais, S. Enouz-Vedrenne, J. Briatico, M. Bibes, A. Barthélemy, and J. E. Villegas, Nanoscale electrostatic manipulation of magnetic flux quanta in ferroelectric/superconductor BiFeO₃/YBa₂Cu₃O_{7- δ} heterostructures, *Phys. Rev. Lett.* **107**, 247002 (2011).
- [72] Y. Lai, Z. Song, Y. Wan, M. Xue, C. Wang, Y. Ye, L. Dai, Z. Zhang, W. Yang, H. Du, and J. Yang, Two-dimensional ferromagnetism and driven ferroelectricity in van der Waals CuCrP₂S₆, *Nanoscale* **11**, 5163 (2019).
- [73] J. Zhang, S. Wu, Y. Shan, J. Guo, S. Yan, S. Xiao, C. Yang, J. Shen, J. Chen, L. Liu, and X. Wu, Distorted monolayer ReS₂ with low-magnetic-field controlled magnetoelectricity, *ACS Nano* **13**, 2334 (2019).
- [74] H. Yang, L. Pan, M. Xiao, J. Fang, Y. Cui, and Z. Wei, Iron-doping induced multiferroic in two-dimensional In₂Se₃, *Sci. China Mater.* **63**, 421 (2020).
- [75] Q. Song, C. A. Occhialini, E. Ergeçen, B. Ilyas, D. Amoroso, P. Barone, J. Kapeghian, K. Watanabe, T. Taniguchi, A. S. Botana, S. Picozzi, N. Gedik, and R. Comin, Evidence for a single-layer van der Waals multiferroic, *Nature (London)* **602**, 601 (2022).
- [76] Y. Wang, P. Wang, H. Wang, B. Xu, H. Li, M. Cheng, W. Feng, R. Du, L. Song, X. Wen, X. Li, J. Yang, Y. Cai, J. He, Z. Wang, and J. Shi, Room-temperature magnetoelectric coupling in atomically thin $\epsilon\text{-Fe}_2\text{O}_3$, *Adv. Mater.* **35**, 2209465 (2023).
- [77] J. Bréhin, Y. Chen, M. D'Antuono, S. Varotto, D. Stornaiuolo, C. Piamonteze, J. Varignon, M. Salluzzo, and M. Bibes, Coexistence and coupling of ferroelectricity and magnetism in an oxide two-dimensional electron gas, *Nat. Phys.* **19**, 823 (2023).
- [78] X. Zhang, J. Liu, and F. Liu, Topological superconductivity based on antisymmetric spin-orbit coupling, *Nano Lett.* **22**, 9000 (2022).
- [79] P. Sharma, T. S. Moise, L. Colombo, and J. Seidel, Roadmap for ferroelectric domain wall nanoelectronics, *Adv. Funct. Mater.* **32**, 2110263 (2022).